Construction and Building Materials 409 (2023) 134082

Contents lists available at ScienceDirect

Construction and Building Materials

journal homepage: www.elsevier.com/locate/conbuildmat

Reactivity of MSWI-fly ash in Mg-K-phosphate cement

Davide Bernasconi [a,*], Alberto Viani [b], Lucie Zárybnická [b], Petra Mácová [b], Simone Bordignon [c], Gangadhar Das [d], Elisa Borfecchia [c], Mateja Štefančič [e], Caterina Caviglia [a], Enrico Destefanis [a], Andrea Bernasconi [a], Roberto Gobetto [c], Alessandro Pavese [a]

[a] Earth Sciences Department, University of Turin, Turin 10125, Italy
[b] Institute of Theoretical and Applied Mechanics of the Czech Academy of Sciences, Centre Telč, Czech Republic
[c] Chemistry Department, University of Turin, Turin 10125, Italy
[d] Elettra Sincrotrone Trieste, 34149 Basovizza, Trieste, Italy
[e] Slovenian National Building and Civil Engineering Institute, Ljubljana, Slovenia

ARTICLE INFO

Keywords:
Municipal solid waste fly ash
Magnesium phosphate cement
Waste reactivity
Stabilization/solidification

ABSTRACT

In this study, the behaviour and reactivity of Municipal Solid Waste Incineration Fly Ash (MSWI-FA), introduced in the formulation of magnesium potassium phosphate cement (MKPC), was investigated by considering the waste either as fully inert or reactive. MSWI-FA induced structural and compositional modifications in MKPC as a consequence of dissolution/precipitation processes which involved many MSWI-FA elements (e.g., Ca, Mg, Al, Si, Zn) and led to the formation of mostly amorphous phosphate secondary products. The reaction path has been described in terms of the early fast dissolution of MSWI-FA, with precipitation of very low solubility phases, and subsequent late precipitation due to pH changes and water subtraction during MKPC gelification. The increase in amorphous content peaked to 50 wt.% and it has been related to the improved behaviour with respect to the leaching of heavy metals (reduced by 70-99%), pointing to this cement as an excellent matrix for their chemical stabilization. The obtained MKPC microstructure exhibited better mechanical performance, with an improvement of up to 60% in compressive strength. All in all, the results indicated that the incorporation in MKPC is a viable recycling opportunity for MSWI-FA, although, for an effective cement formulation, its reactivity must be taken into account.

1. Introduction

Magnesium potassium phosphate cement (MKPC) is commonly classified as chemically-bonded ceramics in which the hardening occurs at room temperature through the acid-base aqueous reaction between an alkaline magnesia source (MgO; periclase) and a source of acid phosphate (KH_2PO_4, KDP), according to the following chemical equation [1]:

$$MgO + KH_2PO_4 + 5H_2O \rightarrow MgKPO_4{\cdot}6H_2O \quad (1)$$

This reaction is fast, exothermic and its mechanism has been described as a multi-step process, which can be summarized in i) MgO dissolution and complexation of cations, ii) formation of an amorphous gel-like phase by interaction with phosphate anion and iii) partial/total crystallization of $MgKPO_4{\cdot}6H_2O$ (K-struvite) in proximity or ~~around~~ at the surface of the unreacted MgO particles [1,2]. As a result, the mechanical strength is ascribable to a network of acicular/platelet-like K-struvite crystals embedded in an amorphous matrix, ~~thus~~ producing a sort of composite material [3,4]. Commonly, formulations in excess of MgO, with respect to the stoichiometry of the reaction in Eq. 1, are employed. Therefore, for Mg/P molar ratio > 1 (usually up to 6–8), the unreacted oxide fraction behaves as a filler, further reducing the porosity of the cement [4,5]. Many studies have discussed the effect of the operational parameters on the reaction kinetics and cement performance: the influence of the M/P ratio; the reactivity of MgO, in terms of particle size and sintering temperature (which can be as high as 1800 °C); the water-to-binder ratio and the use of reaction retarders [4,5–7].

MKP-based cements (MKPC) are the object of an increasing interest because of their excellent properties, such as high early age and long-term strengths, resistance to the sulfate attack, rapid setting, *quasi*-neutral pH, low shrinkage, good water resistance, high adhesive properties [7]. Therefore, they have been proposed for several applications:

* Corresponding author.
E-mail address: davide.bernasconi@unito.it (D. Bernasconi).

https://doi.org/10.1016/j.conbuildmat.2023.134082
Received 7 September 2023; Received in revised form 2 November 2023; Accepted 3 November 2023
Available online 15 November 2023

rapid rehabilitations of infrastructures, waste stabilization/solidification and biomedical materials [6–9]. In the former case, blends with various binding agents or mineral admixtures have been studied, to reduce the cost of raw materials, which limits the use of this class of binders on a large-scale. With the concomitant pressure to mitigate the environmental impact of building materials, coal fly ash (CFA) has represented one of the most exploited solutions [7,10,11]. Coal fly ash is a by-product of coal combustion, and it is characterized by small spherical particle (mean size < 10 μm), high amorphous content (>80 wt%) and an oxide composition rich in SiO_2 and Al_2O_3 [11,12]. The incorporation of coal fly ash in MKPC was found to improves the paste workability and mechanical performance, mainly by physical effects (morphological/microaggregate) [10–13]. Therefore, CFA has been usually considered to behave as inert filler, reducing the heat development, the setting time and the final porosity. However, recent studies have questioned this view, providing evidence of its participation in the MKP formation reaction, although the full structural and chemical information on the related secondary products could not be assessed [10,11]. Similar results were obtained in a study on the impact of coal fly ash and metakaolin on the MKPC's performance, since no changes in the Al and Si networks could be detected by ^{27}Al and ^{29}Si MAS solid state nuclear magnetic resonance (SSNMR) spectroscopy [14].

Unlike coal fly ash, Municipal Solid Waste Incineration fly ash (MSWI-FA) has been much less studied in MKPC. This waste is collected in the incineration plant flue gas purification system and presents significant differences with respect to the counterpart from coal furnaces [15].

MSWI-FA chemistry is dominated by CaO (20–40 %), due to the lime-based scrubber treatment of acidic compounds in the flue gas (i.e., HCl and SO_x), which is the cause of the high concentration of Ca-salts in the ash, in the form of $CaSO_4$ and CaClOH [15–17]. In addition, MSWI-FA displays a significant heterogeneity in terms of particle size and shape (particle size spanning from few μm to 300–400 μm), in contrast with the typically very fine and uniform smooth spherical shape of CFA. This is probably due to the different processing temperature and the high chemical variability of the waste feed, that is also responsible for the presence of heavy metal pollutants (i.e., Pb, Zn, Ni, Cr, Cu).

Many solidification/stabilization (S/S) treatments have been proposed as recycling solutions for MSWI-FA [15,18]. Notable examples are ordinary Portland cement and geopolymers [18–20], in which MSWI-FA is usually pre-treated to reduce ~~it's~~ the salt content. Of the few investigations regarding the incorporation of MSWI-FA into MKPC, Su et al. (2016) focused on the synergistic effect of MSWI-FA in the stabilization of Pb/Cd-loaded MKPC, and demonstrated the good efficacy in the former case, owing to the fly ash's pore-filling and heavy metal adsorption properties [21]. More recently, Yang et al. (2019) tested the performance of MSWI-FA in MKPC different formulations, concluding that 10 % wt. of MSWI-FA is the optimal addition, leading to a 20 % higher 60-day compressive strength and 20 % smaller 60-day shrinkage deformation [22]. To date, no in-depth analysis of the effects of the cement environment (i.e., pH and chemical conditions) on the MSWI-FA reactivity has been provided.

In the present work, the incorporation of washed/steam-washed MSWI-FA into MKPC was studied, focussing on the waste participation in the cement reaction. In particular, the occurrence of dissolution/precipitation reactions involving MSWI-FA components was thoroughly assessed, together with the chemical characterization of the related secondary products. This is thought to contribute to the understanding of the MSWI-FA behaviour in the cement matrix, with the aim of defining the optimal conditions to its recycling. The experiments were designed by taking the *reactivity* of MSWI-FA into account, in terms of MgO "equivalent" [10]. Two formulations will be discussed: in one, MSWI-FA is considered an *inert system*, replacing both MgO and KDP; in the other, MSWI-FA is considered *reactive*, thus replacing MgO only. The suspension of MSWI-FA in a KDP saturated solution has been also studied, in order to obtain further information on the reaction products. The samples under investigation were characterized by X-ray powder diffraction (XRPD), scanning electron microscopy coupled with energy dispersive spectroscopy (SEM-EDS), isothermal conduction calorimetry (ICC) techniques, in addition to compressive strength and leaching performances. The occurrence of significant amorphous components in the cement and MSWI-FA motivated the use of spectroscopic techniques such as SSNMR (on ^{27}Al, ^{29}Si, ^{31}P) and synchrotron Zn K-edge X-ray absorption spectroscopy (XAS).

2. Experimental

2.1. Materials

The raw materials employed in this study were: reagent grade MgO (assay 99.8 %), reagent grade KH_2PO_4 (assay 99.8 %) (Lach-ner s.r.o) and MSWI-FA from an incineration plant located in Turin (Italy). MgO powder was calcinated for 1 h in laboratory furnace at 1500 °C, then milled for 1 min in a Mini-Mill Pulverisette 23 (Fritsch) at 30 oscillations/min. Particle size analysis and specific surface area were conducted in triplicate, resulting in an average particle size d_{50} of 7.2 μm and a BET surface area of 2.98 m^2g^{-1}. MSWI-FA were firstly subjected to a water/steam-washing treatment (liquid-to-solid ratio of 10, time of treatment of 24 h, steam flux of 2 L/min, humidity of 40 % v/v, time of treatment of 10 min) to reduce the content of soluble phases and heavy metal leaching [23,24]. Then, the washed ash was filtered, ground in a mortar (RM 200, Retsch, Germany) and sieved to a size < 63 μm. The chemical compositions of the raw materials were determined by X-Ray Fluorescence measurements and are reported in Table 1.

2.2. Formulation design

The formulation details of the investigated MKPC pastes are reported in Table 2. Although it is usually applied in commercial mixes, the retarder addition was here avoided because the objective was to explore the reactivity of MSWI-FA in the pure MgO-KH_2PO_4 system. A MgO/KH_2PO_4 (M/P) molar ratio of 1.75 and water-to-binder weight ratio (*w*/b) of 0.45 were used [1,2], to favour the dissolution of MSWI-FA particles and resulting cations/anions mobilization. The ash residue was implemented at a fixed 30 wt% MgO with respect to the reference formulation (REF). Such value was chosen as it allows to observe the MSWI-FA behaviour without altering too much the main cement reaction [10]. In the case of the *inert* formulation (MF0), the ash was simply added as a filler, without being considered part of the binder; for the *reactive* formulation (MF100), the waste partially substituted MgO. A fixed *nominal* M/P of 1.75 and fixed water-to-*nominal* binder ratio of 0.45 were considered to calculate KH_2PO_4 and water content. An additional sample (MSWI-FA/KDP) was investigated to estimate the potential reactivity of the ash. It consists of a MSWI-FA diluted (at liquid-to-solid ratio of 2) suspension in KH_2PO_4 saturated solution (obtained by dissolving 7 g of salt in 50 ml of ultrapure water).

2.3. Analytical methods

The phase composition was determined by XRPD measurements using a Miniflex 600 diffractometer (Rigaku, Japan), with Cu-Kα incident radiation and operated at 40 kV–15 mA. XRPD patterns were collected between 5° and 70° 2θ, with a 2θ-step size of 0.02 and scan speed of 0.5°/min. The Rietveld analysis, using high purity ZnO as an internal standard (10 wt%), was employed to determine the MSWI-FA and cement pastes mineralogical composition and amorphous content [1,2]. The Rietveld strategy involved the refinement of 14 Chebyshev polynomial background coefficients, 2θ-zero parameter, cell parameters, phase fractions, isotropic crystal size of each phase, together with Mach-Dollase correction for preferred orientation when necessary (es., gypsum and brushite) [17]. Data refinements were carried out by the software GSASII [25].

Table 1
Chemical composition (wt %) and main physical properties of MSWI-FA. Uncertainties of about 2–3%.

Raw materials	Chemical composition (wt %)										BET (m^2g^{-1})	D_{50} (μm)	D_{90} (μm)
	Al_2O_3	Fe_2O_3	TiO_2	K_2O	CaO	SiO_2	MgO	SO_3	P_2O_5	Others			
MSWI-FA	7.37	8.99	2.87	0.45	44.38	22.51	6.98	5.23	0.38	0.86	15.7	8.8	29.1

Table 2
Formulations of MKPC pastes.

	REF	MF0	MF100
	(g)	(g)	(g)
MgO	350	350	245
MSWI-FA	–	105	105
KDP	675	675	675
Water	461	461	461

All SSNMR measurements were recorded at room temperature on a solid-state NMR spectrometer (JNM-ECZ600R, JEOL RESONANCE Inc., Japan) with a magnetic field of 14.1 T, operating at ^{1}H, ^{27}Al, ^{29}Si, and ^{31}P Larmor frequencies of 600.1, 156.4, 119.2, and 242.9 MHz, respectively. The samples were packed into 3.2 mm zirconia rotors and spun at a MAS frequency of 15 kHz, 15 kHz and 20 kHz for ^{27}Al, ^{29}Si, and ^{31}P MAS spectra, respectively. A pulse of 12 μs, 4 μs and 3 μs, with relaxation times of 10 s, 10 s and 20 s, were set for ^{27}Al, ^{29}Si and ^{31}P nuclei, respectively. ^{31}P CP/MAS spectrum was collected with a contact time of 3 ms and relaxation delay of 1 s. ^{1}H, ^{27}Al, ^{29}Si, and ^{31}P chemical shifts scales were referenced through the resonances of adamantane, aluminium nitrate, silica and $(NH_4)H_2PO_4$, respectively. The spectra deconvolution analysis was carried out using the built-in feature of Delta 6.1 (Jeol), by employing pseudo-Voigt functions, while the estimated uncertainty on the determined fractions is in range of ± 1 %.

Secondary electron (SE) and back scattered electron (BSE) images were collected by a Scanning Electron Microscope JSM IT300LV High Vacuum – Low Vacuum 10/650 Pa – 0.3–30 kV (JEOL USA Inc.), operating at the following conditions: W filament, EHT 15 kV, standard probe current and working distance 7 mm for images and high probe current and working distance 10 mm was employed for chemical analysis in energy dispersive (EDS) mode. SEM-EDS and BSE images of washed MSWI-FA and MSWI-FA/KDP sample were collected by a Tescan Vega (operating at 10 and 15 kV and beam current of 20 and 300 pA for imaging and chemical analysis, respectively).

Compressive strength tests were performed on 28-days cured MKPC cubes (1x1x1 cm), measuring 3 replicates by means of an Instron 3345 (Instron, USA) loading frame, at loading speed of 0.2 mm/min and 5 N load cell.

Isocalorimetry experiments were conducted with a TAM-Air (TA Instruments) 8-channel instrument. For each formulation (both cements and suspension), the powder and the liquid were kept separated in an Ad-Mix® ampoule until both were equilibrated at the measurement temperature (20 °C). The liquid was manually injected onto the powder, defining the start of the experiment. The slurry was mixed for 30 s and the heat flow was recorded for 10 h.

The batch (static) leaching tests, according to EN 12457–2, 2002, was employed for MSWI-FA and cement samples [26]. Prior to the test, cement cubes were ground and sieved to obtain a powder with particle size less than 1 mm. The test involves the immersion of the powdered samples in ultrapure water solution at natural pH, with a liquid-to-solid ratio set to 10 and 24 h shaking. Then, the resulting suspension was filtered, and the leachates recovered for Inductively-Coupled-Plasma Mass-Spectroscopy (ICP–MS) measurements, using an Agilent 7500 ICP-MS. The solution samples were first filtered through a 0.45 μm pore size membrane, then acidified using a concentrated HNO_3 solution and analysed. Accuracy and precision, based on replicated analyses on standards, were estimated as better than 10 % for all elements, *i.e.* above the detection limit.

The Zn K-edge XAS spectra of the samples were collected at at the XRF Beamline of Elettra Synchrotrone Trieste (Italy). All samples were finely ground, and 13 mm-diameter pellets were prepared using ca. 150 mg of sample, to be measured in fluorescence mode. The Zn K-edge XAS spectra of reference minerals samples were all collected in transmission mode, at the XAFS beamline of Elettra, by calculating the optimal mass for an absorption jump around 1 and mixing the calculated amount of sample with boron nitride to reach 100 mg for the pelletization. Zn K-edge XAS spectra were collected using a Si(1 1 1) double crystal monochromator, while Zn foil was used as a standard for energy calibration to 9659 eV. A number of scans ranging from 3 to 5 was collected for samples, while 1 to 2 scans were acquired for reference minerals; the corresponding μ(E) curves were averaged after checking for signal reproducibility. The XAS spectra were collected with an energy step of 5 eV in the pre-edge region, of 0.2 eV in the near-edge region (XANES) and a constant k step of k = 0.035 $Å^{-1}$ in the extended fine structure region (EXAFS). Energy alignment and normalization to the edge-jump as well as XANES Linear Combination Fitting (LCF) analysis were performed by using the DEMETER open-source package (ATHENA) [27].

3. Results

3.1. Isocalorimetry (ICC)

The first 50 min of the heat flow (normalized to the amount of MgO) produced during the cement reaction at 20 °C is shown in Fig. 1 (top). The REF sample displays the typical curve observed in similar pure formulations [1]. An initial endothermic peak is recorded immediately after mixing (Fig. S1), related to the dissolution of KH_2PO_4, which is usually neglected as it is of very low intensity and largely masked by the following two more intense exothermic events. The first one has been assigned to the dissolution of MgO, while the second, characterised by a much broader exothermic peak, relates to the crystallization of MKP [1]. When the normalized heat flow curve of the inert MF0 formulation is considered, no significant differences in terms of time and intensity can be observed for the MgO dissolution. Interestingly, a change is apparent on the MKP crystallization peak, whose maximum starts earlier (10 min with respect to 13 min for REF0) and, in general, appears to be sharper, thus more 'compressed' in time, indicating an increase of the reaction kinetics of the overall process. On the contrary, MF100 presents a clear delay of the maximum of the MgO dissolution peak (6 min against 5.3 min for REF0). Accordingly, the normalized total heat curve evidenced for MF100 a significant higher amount of heat released at the end of the experiments, while REF0 and MF0 are very close (1720 J/g against 1425 and 1410 J/g, respectively). Notably, most of the difference with REF0 and MF0 is concentrated in the first 10–15 min, confirming the predominant contribution from MgO dissolution.

In order to better isolate the potential MSWI-FA contribution to the total exchanged heat and heat flow, an additional experiment has been conducted, where MSWI-FA was mixed with a saturated solution of KH_2PO_4 (liquid-to-solid ratio of 2) inside the calorimeter (Fig. 1, inset). The heat release curves confirmed the reaction of the MSWI-FA in the acidic environment, although the intensity of the maxima, normalized to the amount of MSWI-FA, are about one order of magnitude lower with respect to the cement samples' (0.1 against 1.2 W/g and 74 against 1400–1700 J/g, respectively). The time scale of the heat flow peak, going to completion in about 40 min, is compatible with the fast kinetics typical of the acid-base reactions [28].

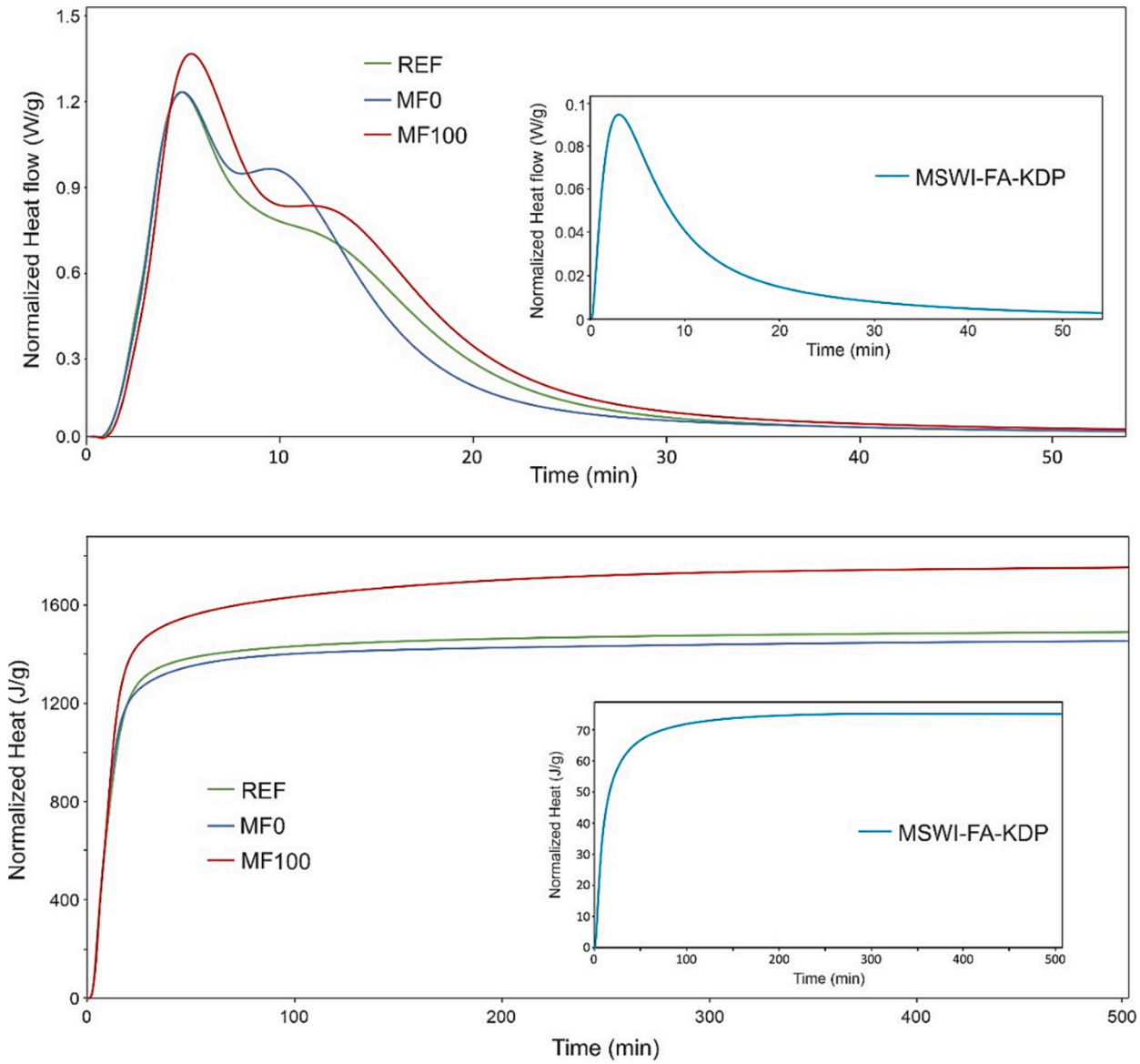

Fig. 1. Normalized heat flow (top) and total heat (bottom) of cement mixtures. MSWI-FA/KDP suspension curves are represented in the insets.

3.2. X-ray powder diffraction (XRPD)

The XRPD patterns of MSWI-FA and cement pastes are shown in Fig. 2. MSWI-FA, after washing treatment, exhibits a complex mineralogy, including sulfate phases (gypsum, anhydrite and ettringite), quartz, calcite, melilite, perovskite, together with a significant amount of amorphous fraction [16,17]. In the REF sample, the only crystalline phases are represented by K-struvite, along with a residual periclase (MgO), as expected considering the used M/P molar ratio (1.75:1), whereas KH_2PO_4 is not detected. In the case of MF0 and MF100 formulations, additional peaks of quartz and anhydrite related to MSWI-FA are present, together with calcite. Low intensity peaks of arcanite (K_2SO_4) are visible, suggesting a release of sulfate from MSWI-FA. The results of the Rietveld quantitative phase analysis of the pastes are reported in Table 3, while an example of the graphical output for MF0 is illustrated in Fig. S2. As previously observed, the typical cement products consist of both crystalline and amorphous MKP [1,2]. With respect to the REF sample, MF0 does not exhibit a significant decrease in residual MgO, while a much higher proportion of the amorphous precursor remains after the experiment (26.7 wt% against 51.6 wt%). A similar amorphous fraction is also present in MF100 (40.1 wt%).

As a comparison, the phase composition of the sample MSWI-FA/KDP collected after isocalorimetry is shown in Table 4, to emphasize the potential MSWI-FA mineralogical transformations that may occur during the cement reactions. It is apparent that even in this case, some calcite is still present, in agreement with the results of the cement pastes, while a more effective dissolution involved other phases, like ettringite and periclase. In a similar way, arcanite is observed, together with the crystallization of Ca-phosphate (brushite). The marked decrease of anhydrite can be in part explained with its hydration to gypsum, whose content increased (1.6 to 4.3 wt%), because of the diluted environment [29]. Moreover, it is also likely that anhydrite, as well as ettringite dissolution may have provided the ions for the precipitation of arcanite and brushite. It is worth noting that the amorphous content increased by 50 % (from 53.4 to 77.1 wt%), indicating that most of the secondary products are poorly crystalline/x-ray diffraction amorphous.

3.3. Solid-state NMR (SSNMR)

The ^{31}P MAS spectra of the cement samples are shown in Fig. 3. All spectra are dominated by a peak at 6.3 ppm, related to the crystalline MKP. The broader signal centred at around 2.1 ppm of much lower

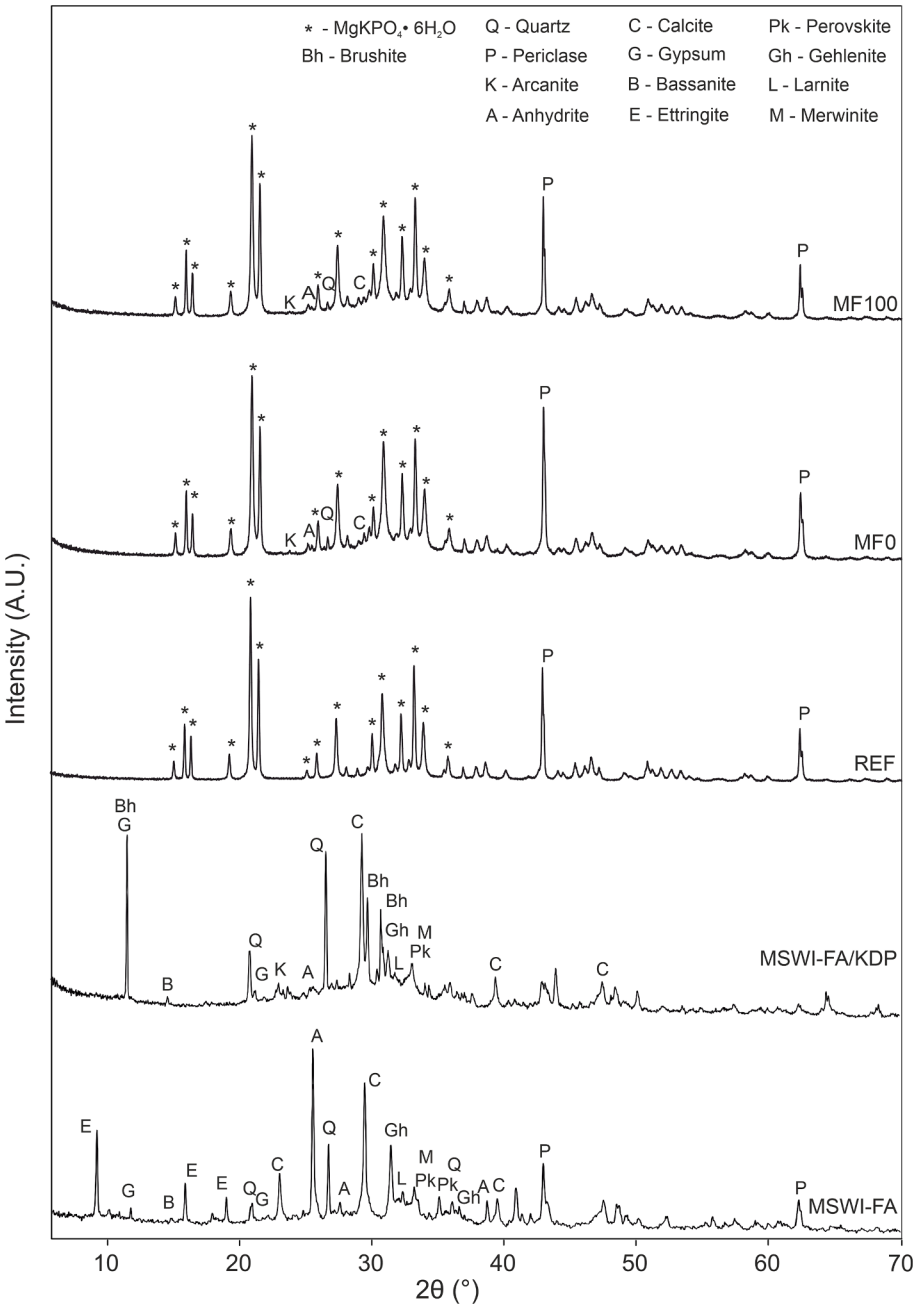

Fig. 2. XRPD patterns of cement pastes, together with MSWI-FA and MSWI-FA/KDP sample.

Table 3
Results of quantitative phase analysis with the internal standard method of samples 28 days after the reaction in the calorimeter at 25 °C. The uncertainties are ± 0.1 wt% (crystal phases) and ± 2 wt% (amorphous phase).

Sample	REF	MF0	MF100
	wt%	wt%	wt%
MKP	65.6	40.1	52.9
Periclase	8.1	7.4	5.1
Quartz	–	0.2	0.2
Calcite	–	0.3	0.3
Anhydrite	–	0.2	0.2
Arcanite	–	0.2	0.2
Amorphous	26.3	51.6	41.1

intensity has been assigned to the cement amorphous precursor [2]. A signal deconvolution approach was employed, to better evaluate differences between the samples. The broad amorphous contribution has been modelled using two components, which are related to previously identified two distinct amorphous orthophosphate environments, which exhibit different dynamics under cross-polarization conditions [1,2]. It is apparent that the MSWI-FA cement samples present a lower MKP crystalline/amorphous ratio with respect to REF, especially MF0, in accordance with XRPD results (Table 3).

In addition, with respect to the neat MKPC (REF sample), a contribution to the amorphous component from MSWI-FA might be present. Indeed, the MAS spectrum of MSWI-FA/KDP (Fig. 4, bottom) exhibits a sharp resonance at around 1.3 ppm, assigned to brushite, but it is dominated by a significantly broader asymmetric peak that spans from 7 to −12 ppm. The $^{31}P\{^{1}H\}$ CP/MAS experiment (Fig. 4, top) produced mainly the brushite peak and a secondary much smaller resonance at

Table 4
Results of quantitative phase analysis with the internal standard method of MSWI-FA and MSWI-FA/KDP. The uncertainties are ± 0.1 wt% (crystal phases) and ± 2 wt% (amorphous phase).

Sample	MSWI-FA	MSWI-FA/KDP
	wt%	wt%
Quartz	3.2	3.3
Calcite	11.9	5.1
Anhydrite	9.2	1.3
Larnite	1.5	0.8
Gehlenite	2.9	1
Periclase	4.5	–
Gypsum	1.6	4.3
Bassanite	0.2	0.1
Ettringite	9.6	–
Merwinite	0.9	0.6
Perovskite	1.1	0.8
Arcanite	–	3.8
Brushite	–	2.6
Amorphous	53.4	77.1

around −7 ppm, possibly related to newberyite ($MgHPO_4{\cdot}3H_2O$) could be identified. Since in the $^{31}P\{^1H\}$ CP/MAS experiment magnetization is transferred from the neighbouring protons, emphasizing the signal from ^{31}P nuclei in close proximity to protons, the spectra point to identify most of the amorphous products as either orthophosphate or pyrophosphate with no significant interaction with ^1H nuclei [11,30].

^{27}Al and ^{29}Si MAS experiments are of interest to get insights into the behaviour of MSWI-FA, as it represents the only source of these nuclei in the mixtures. ^{27}Al MAS spectra of all samples are shown in Fig. 5, together with the raw ash. The MSWI-FA spectrum displays a broad peak at around 68 ppm, which is related to the tetrahedral Al(IV) speciation in the aluminosilicate glass fraction, a narrow peak at around 13 ppm assigned to $Ca_6Al_2(SO_4)_3(OH)_{12}{\cdot}26H_2O$ (ettringite) [31] and a broader resonance centred at 9.5 ppm originated by a limited fraction of octahedral Al(VI) in aluminosilicate glass or amorphous aluminium hydroxide phases [32].

When MF spectra are considered in Fig. 5, significant differences are apparent in the octahedral region. In particular, the ettringite signal

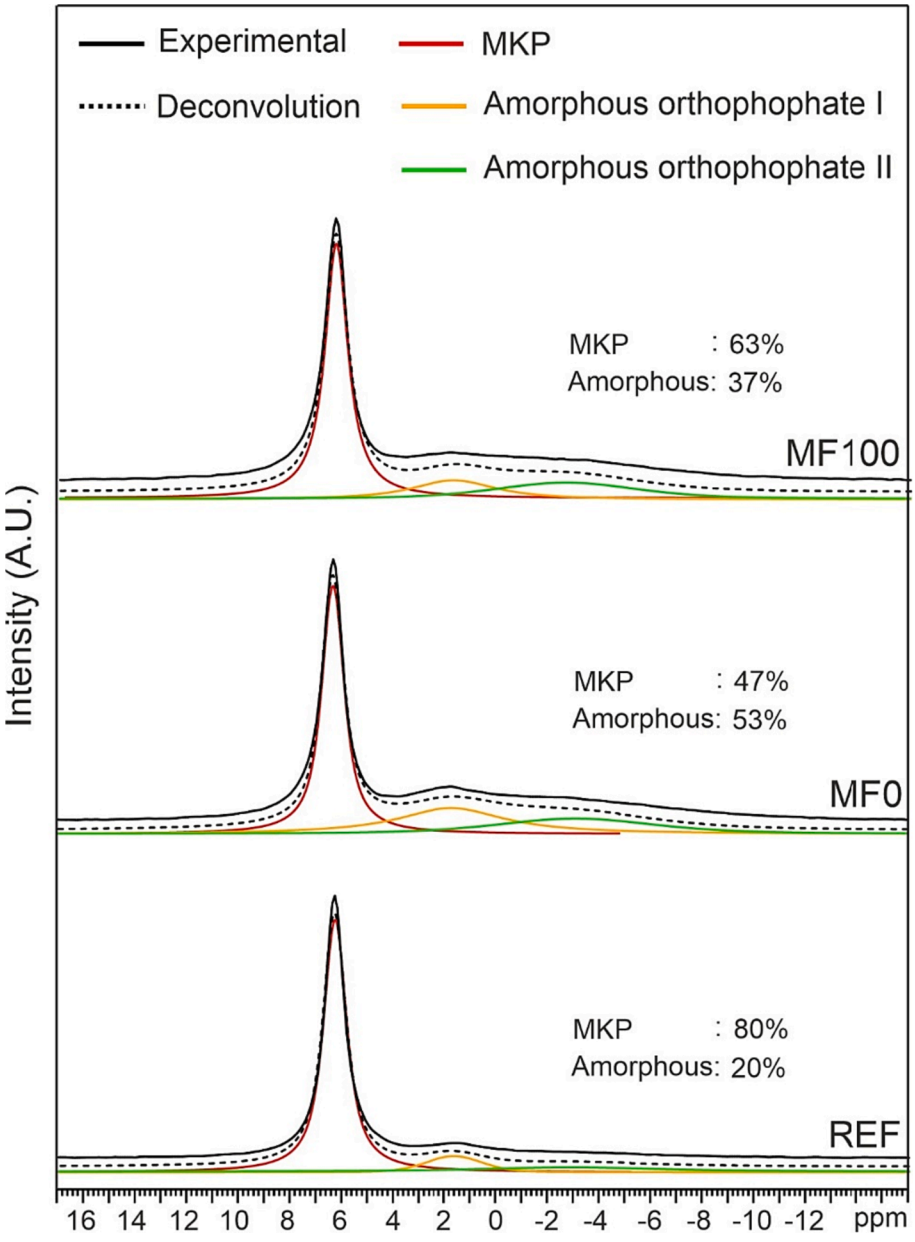

Fig. 3. ^{31}P MAS spectra of cement samples.

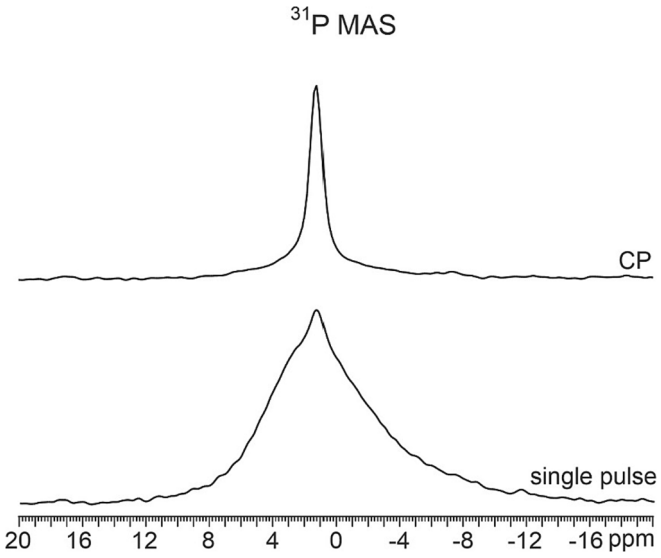

Fig. 4. ^{31}P MAS and ^{31}P{^{1}H} CP/MAS spectra of MSWI-FA/KDP sample.

markedly reduces and a new broad peak develops at around −12 ppm. Moreover, the Al(IV) aluminosilicate glass displays an increased linewidth, which may indicate partial dissolution or alteration [11]. The new Al(VI) signal should be related to some secondary product involving MSWI-FA. Indeed, a very similar profile is observable for the MSWI-FA/KDP sample, where this signal is even more apparent (Fig. S3). The analysis has been also conducted from a semi-quantitative standpoint through spectra deconvolution. Graphical results are illustrated in Fig. S4. The ettringite signal accounts for around 23 % of Al in MSWI-FA, decreasing down to 7 % in MF0 and disappearing in MF100. A slight decrease also involved the amorphous Al (IV) peak, while the new resonance at negative ppm become more significant in the reactive formulation (22 % and 36 % in MF0 and MF100, respectively).

^{29}Si chemical shift is particularly sensible to the coordination number and nature of second coordination sphere atoms. In particular, SiO_4 tetrahedra are represented by Q^n (n = 0, 1, 2, 3, 4), where n is the number of bridging oxygens, and their shifts are − 60 to − 81 ppm (Q^0), −68 to − 83 ppm (Q^1), −74 to − 93 ppm (Q^2), −91 to − 101 ppm (Q^3), and − 102 to − 118 ppm (Q^4) respectively [32]. When Si atoms are replaced by Al atoms, the Si-O-Al units are usually expressed as Q^n(mAl) (m, n = 1, 2, 3, 4), and their chemical shift ranges for Q^4(1Al), Q^4(2Al), Q^4(3Al), Q^4(4Al) between − 96 to − 105 ppm, −91 to − 99 ppm, −85 to − 94 ppm, and − 81 to − 91 ppm, respectively [32].

^{29}Si MAS spectrum of MSWI-FA (Fig. 5, right) is characterized by a very broad peak between −60 and −120 ppm, which encompasses all the different silicate/aluminosilicate environments present in the residue, spanning from the less reticulated Q^0 (i.e., larnite, see Table 4), Q^1 (i.e., gehlenite) and Q^2 units at −63, −72 and −80 ppm, respectively, to

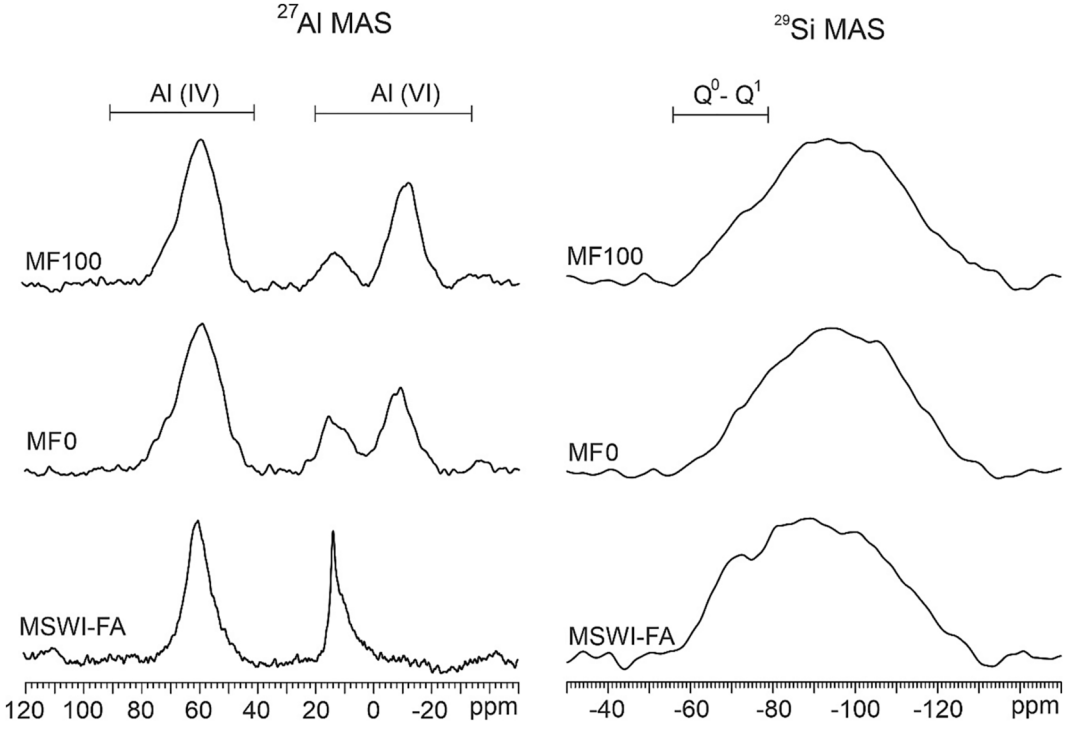

Fig. 5. ^{27}Al (left) and ^{29}Si (right) MAS spectra of MSWI-FA and cement samples.

the higher cross-linked Q^4(mAl) units of the amorphous glass fraction (from −88 to −113 ppm) [32]. MF0 and MF100 exhibit a similar broad profile, which significantly limits the interpretation and quantification [32]. Nonetheless, a deconvolution approach has been attempted also in this case, by fitting the spectra with the aforementioned contributions (Fig. S5). The MF spectra seem to display a relatively less intense region at higher ppm (-60 to −80 ppm) with respect to MSWI-FA. This is confirmed by the deconvolution, which shows a significant reduction (20–30 %) of the components from the less reticulated Si (Q^0-Q^2), compensated by an increase of the Q^4(0Al) contribution, typical of (amorphous) silica [11,32].

3.4. X-ray absorption spectroscopy (XAS)

Zn K-edge XAS has been employed to get a insights into the mobilization and reactivity of the most abundant MSWI-FA heavy metal (around 1 wt%) [19]. The XANES spectra of MSWI-FA and MF samples, are shown in Fig. 6, while the full XAS profiles, together with those from references samples, are plotted in Fig. S6. Some differences before and after the cement reaction are apparent, namely, a relative increase of the white line intensity and the appearance of an additional feature around 9675 eV, while MF0 and MF100 samples display very similar profiles. A more detailed analysis was performed using the Linear Combination Fitting (LCF) method, which employs a set of known standards to model and fit the spectrum profile [33,34]. All XANES spectra have been modelled using four contributions, which were found enough to account for all the observed features. On average, the R-factor of around 0.02, which translated into an error of ± 3 % on the quantitative data, was considered acceptable [35]. The washed MSWI-FA Zn (Fig. 6) was found to be present as Zn^{2+} in tetrahedral coordination, with a local environment approximated with Zn-aluminate nanospinel (41 %) and Zn-silicate, Zn_2SiO_4 (25 %), together with ZnO (16 %) and hydrozincite (18 %). Both MF samples display similar Zn-aluminate components, but significant differences in the others are present. A decrease of ZnO contributions is evident (11 %), together with the disappearance of hydrozincite. The new observed feature is modelled using a Zn-phosphate, namely hopeite ($Zn_3(PO_4)_2{\cdot}4H_2O$), which becomes one of the main contributions to the XANES profile (29–32 %). Interestingly, a not-negligible reduction of Zn-silicate is also noticeable (16–18 %).

3.5. Morphology (SEM)

The cement samples microstructure (Fig. 7) is mostly determined by the growth of large (above 30–50 μm) and packed K-struvite crystals embedded in an amorphous matrix that exhibits a similar chemical composition (i.e., similar contrast in BSE images). In the MSWI-FA containing samples, arcanite is sometimes partly coating the K-struvite crystals. In pure cement, K-struvite is known to exhibit both platelet-like and prismatic elongated crystal morphology, depending on crystallization rates and conditions (usually, lower reaction rates favour the platelet-like habit) [36]. This seems the case for MF100 with respect to MF0 (Fig. S7), in agreement with the ICC curves (Fig. 1).

MSWI-FA is characterized by a significant heterogeneity in terms of particles shape and chemistry, as shown in Fig. S8. The MSWI-FA/KDP sample is mainly composed by large aggregates (>100–150 μm, Fig. 8, top), where, together with unreacted spherical particles, elongated crystals of Ca-phosphate are recognizable. Interestingly, the EDS spectrum of the bulk phase mostly presents Al, Si and P, suggesting the development of an aluminophosphate binding phase. Moreover, crystals with MKP characteristic platelet habit are observed in association with arcanite (Fig. 8, bottom). As an example, MF0 cross-section BSE image is shown in Fig. 9, together with corresponding EDS map. Overall, the MSWI-FA grains seem to be well embedded in the cement matrix. Indeed, K-struvite growth on spherical particles is noticed in Fig. S9. Arcanite appears between K-struvite crystals, while in this case no clear Al and Si dissolution is observed from the EDS map of the

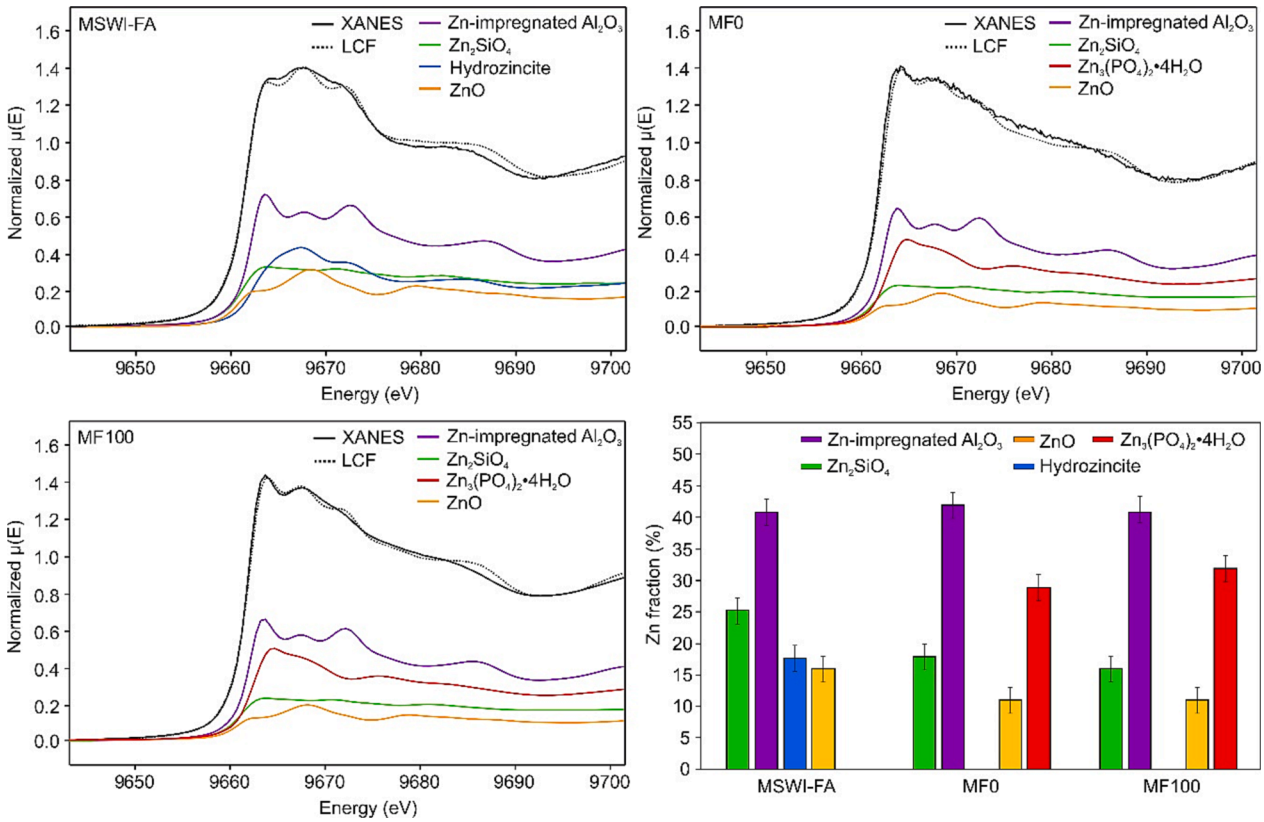

Fig. 6. Zn K-edge XANES spectra of MSWI-FA and MKP samples, with LCF results.

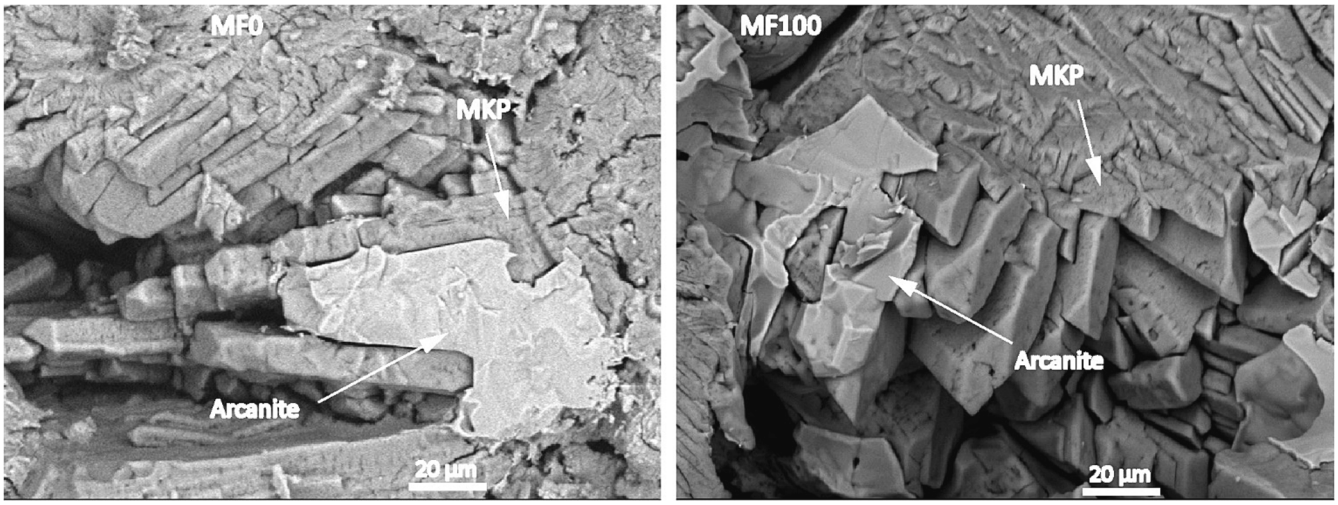

Fig. 7. BSE images of MF0 (left) and MF100 (right).

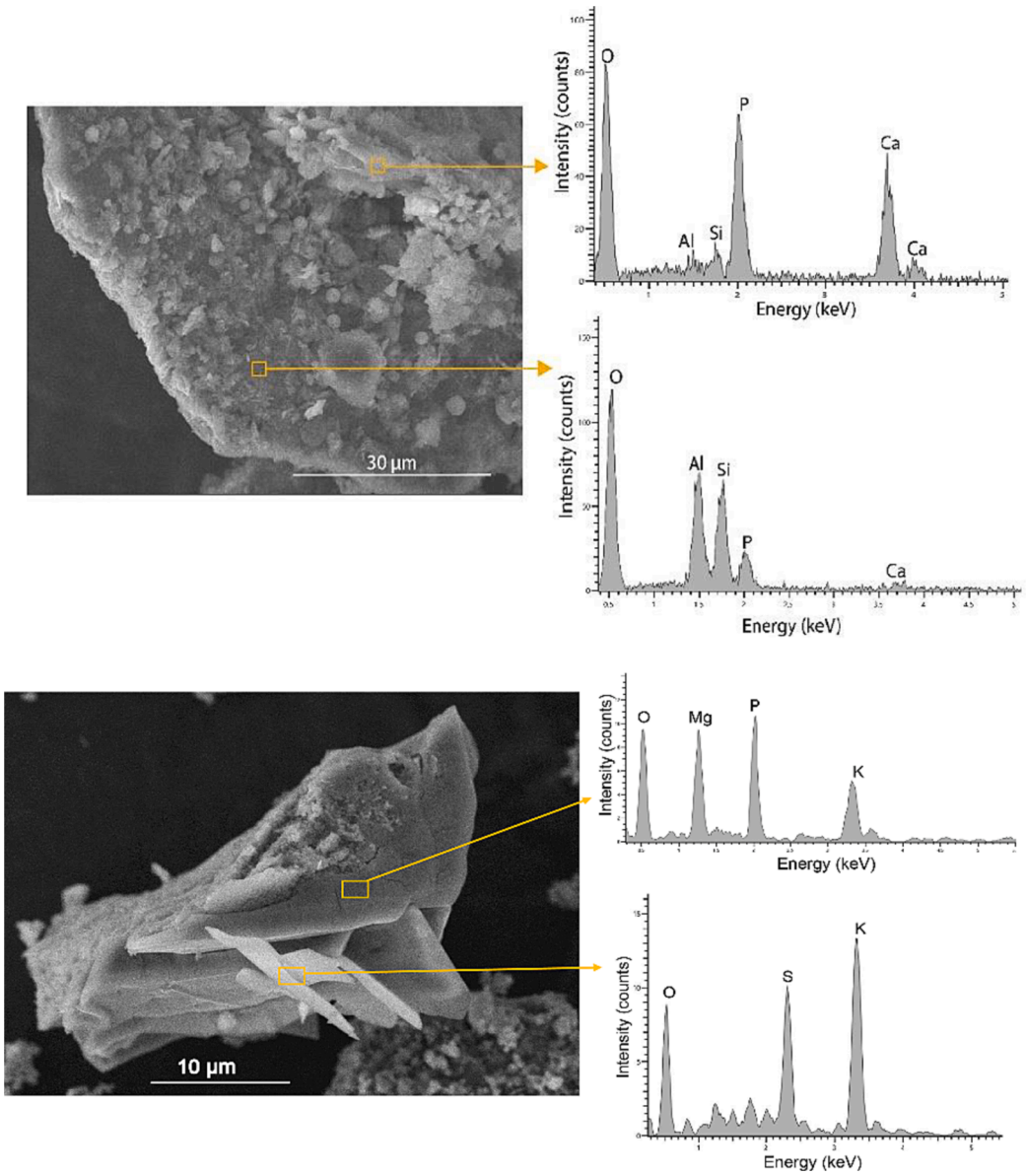

Fig. 8. SE images of MSWI-FA/KDP sample, with EDS spectra.

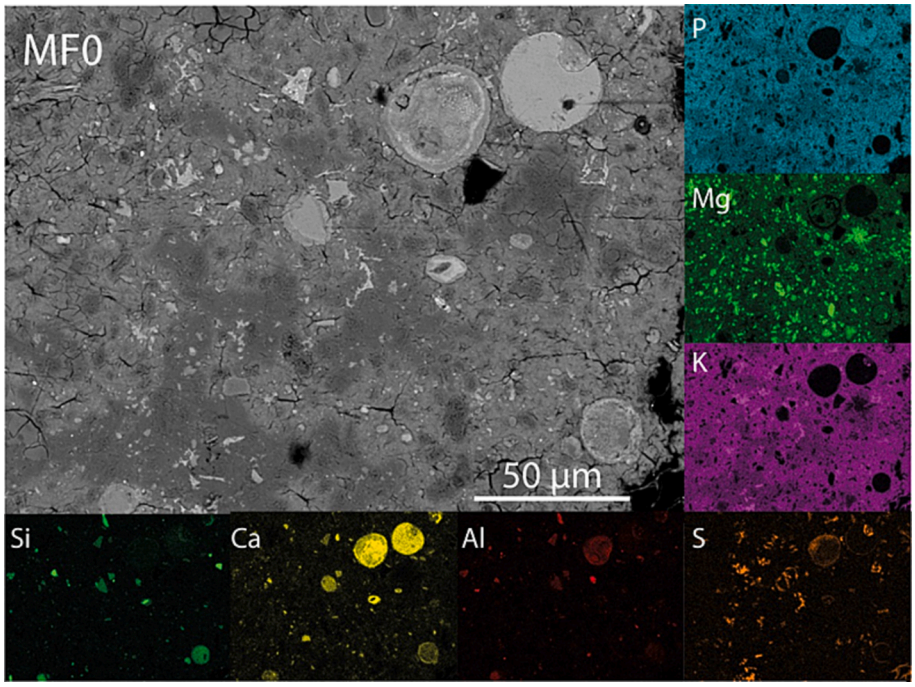

Fig. 9. BSE image of MF0 cross-section, with EDS map.

aluminosilicate grains, possibly due to the limited extension of their reaction rims [11,37]. On the other hand, a closer inspection of the matrix chemistry seems to suggest an enrichment in Al, Si and Ca in the region surrounding MSWI-FA particles (Fig. 10). Additional SEM micrographs and corresponding elemental distribution EDS maps are provided in Figs. S11 and 12.

3.6. Mechanical properties and leaching performance

The compressive strengths of the MKPC samples cured for 28 days are illustrated in Fig. 11 (top). REF and MF0 display comparable values (9.2–10.1 MPa), while a marked increase is visible for MF100 (15.5 MPa). These values may be considered satisfactory for application as an underground mine filling slurry and backfill material [8]. Here, the relatively high water-to-binder ratio of 0.45, the lack of retardant and the use of analytical grade MgO may explain the relatively low values

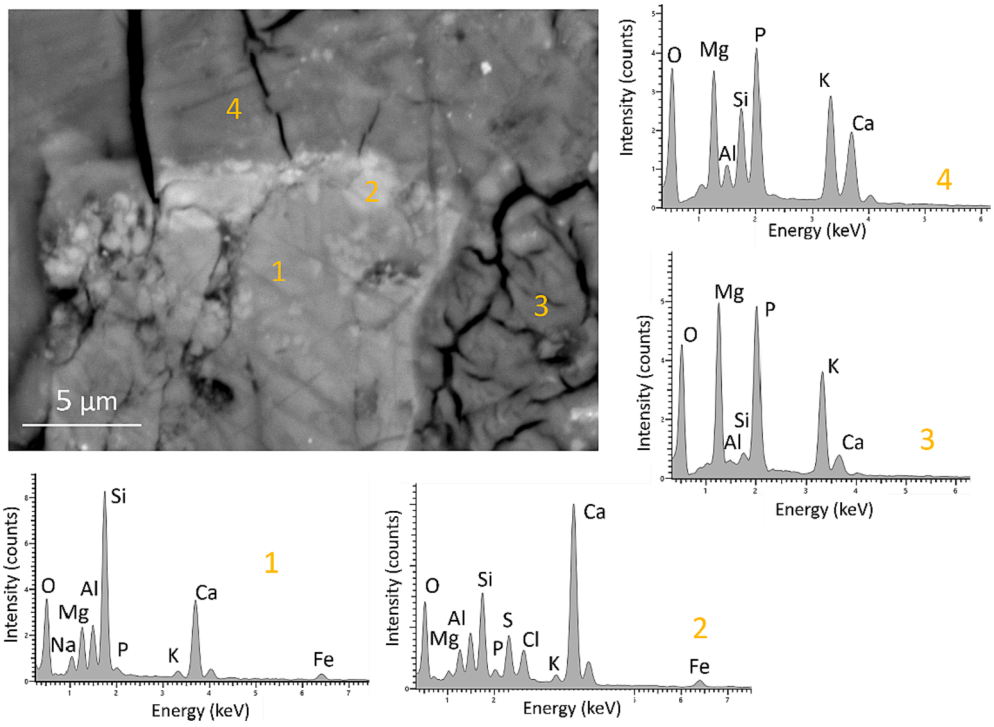

Fig. 10. Details of MF0 cross-section, with EDS spectra.

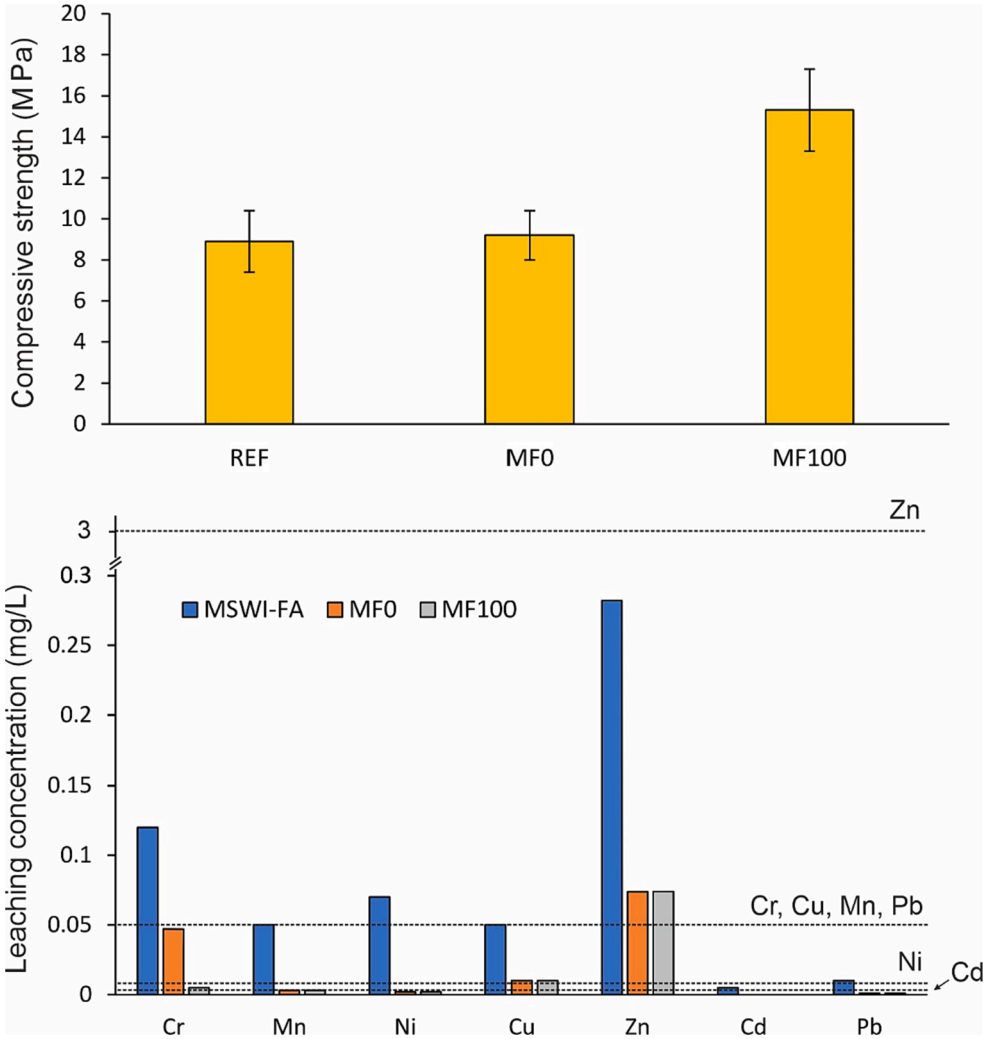

Fig. 11. 28-days compressive strength values of cement samples (top); Leaching test performances, together with MSWI-FA (bottom). The dashed lines represent the law limit according to [39].

observed with respect to the literature [10–13]. Indeed, comparable values were recently reported for MKPC formulated with similar parameters [8,38]. Although the employed formulations are not optimized for mechanical performance, they still represent the typical MKP chemical environment that can be involved in the MSWI-FA S/S process.

The leaching tests of the employed MSWI-FA and related MF samples are set out in Fig. 11 (bottom). Although the waste residue underwent a washing pre-treatment, residual leaching of Zn, Cu, Ni and Cr was observed. It is known that water washing methods are very effective in removing salts (i.e., chloride) from MSWI ashes, while the release of heavy metals may require additional treatments to be fully minimized [18,24]. Here, it is apparent that a marked decrease on all investigated heavy metals leaching below the limits defined for inert waste in Italy, was obtained, in terms of 70–99 % [39]. It is also worth noting that no significant differences are evident between the two formulations, with the exception of Cr.

4. Discussion

4.1. MSWI-FA reactivity

The behaviour of a waste in a binder is dictated by both the chemical/mineralogical composition of the former and the chemical environment of the latter. MKPC develops through the initial dissolution of MgO in acidic environment (pH usually around 4), followed by hydration/precipitation reactions that increase the pH in time, usually up to 8–9 [2,5,28]. MSWI-FA is characterized by a complex phase composition, reported in Table 4. The solubility of the MSWI-FA's main phases (i.e., carbonate and sulfates) is promoted at pH < 6 [12,39]; therefore, their dissolution at the beginning of the cement reaction may provide cations (i.e., Ca^{2+} and Al^{3+}) and contribute to the precipitation of secondary products. Moreover, periclase (4.5 wt%), together with a significant fraction of amorphous, are likely involved in this process.

This was confirmed by the heat released (Fig. 1) and the precipitation of Ca-phosphate (brushite) and MKP when MSWI-FA was allowed to react with the phosphate solution (Fig. 8). The ^{31}P SSNMR analysis on MSWI-FA/KDP sample clearly indicated the formation of different phosphate (Fig. 4), mostly amorphous in nature, as also suggested by the increase of the amorphous amount with respect to MSWI-FA. We observed a similar behaviour by adding the same MSWI-FA in metakaolin phosphate geopolymers [19]. In that case, the ash reactions speeded up the hardening process compared to the pure geopolymer, which has slow kinetics, and the pH remains highly acidic [19]. In MKPC, the system evolves much faster, as shown in Fig. 1, where, for the sample REF, the maximum of the first exothermic peak was reached in 5 min.

The quick change of pH, combined with the relatively high acid neutralization capacity of the MSWI-FA [17], may be responsible for the incomplete calcite dissolution, both in the MSWI-FA/KH_2PO_4 suspension and in the MF0/100 samples. The partial dissolution of the

Table 5
Summary of the observed and proposed reactions and secondary products involving MSWI-FA components.

MSWI-FA component	Possible reaction	Product
Calcium	Dissolution of $CaCO_3$ (calcite)	$CaHPO_4{\cdot}2H_2O$ (brushite)
	Dissolution of $CaSO_4$ (anhydrite)	Amorphous Ca-phosphate
	Dissolution of $Ca_6Al_2(SO_4)_3(OH)_{12}{\cdot}26H_2O$ (ettringite)	Substitution of Mg in MKP
	Dissolution of $Ca_2Al(Al,Si)_2O_7$ (gehlenite)	
Magnesium	Dissolution of MgO (periclase)	$MgHPO_4{\cdot}3H_2O$ (newberyite)
		Amorphous Mg-phosphate
		$MgKPO_4{\cdot}6H_2O$ (MKP)
Zinc	Dissolution of ZnO (zincite)	$Zn_3(PO_4)_2{\cdot}4H_2O$ (hopeite)
	Dissolution of $Zn_5(CO_3)_2(OH)_6$ (hydrozincite)	
	Dissolution of Zn_2SiO_4 (willemite)	
Aluminum	Dissolution of $Ca_6Al_2(SO_4)_3(OH)_{12}{\cdot}26H_2O$	Amorphous Al-phosphate
	Dissolution of $Ca_2Al(Al,Si)_2O_7$ (gehlenite)	
	Dissolution of amorphous aluminosilicate	
Silicon	Dissolution of $Ca_2Al(Al,Si)_2O_7$ (gehlenite)	Amorphous silica
	Dissolution of Zn_2SiO_4 (willemite)	
Sulfate	Dissolution of $CaSO_4$ (anhydrite)	K_2SO_4 (arcanite)
	Dissolution of $Ca_6Al_2(SO_4)_3(OH)_{12}{\cdot}26H_2O$ (ettringite)	

abundant sulfate (i.e., gypsum, anhydrite, ettringite), together with the rapid subtraction of water due to the gelification of the MKP amorphous precursor, have realized the supersaturation conditions required for the precipitation of arcanite (K_2SO_4). Its late precipitation is confirmed by the SEM observation (Fig. 8), where anhedral crystals are filling spaces between the euhedral to subhedral MKP individuals. Concomitantly, the released Ca can substitute Mg in the MKP, as shown in Fig. S8 [8].

There are evidences that also the aluminosilicate fraction of MSWI-FA reacted in the cement chemical environment. The phase composition of MSWI-FA/KH_2PO_4 points to a significant decrease in gehlenite ($Ca_2Al(AlSiO_7)$) content, while the ^{27}Al MAS spectrum clearly shows the presence of a new resonance in the octahedral region at −12 ppm, together with an increase linewidth of the tetrahedral Al (Fig. S4). This is compatible with the incorporation of at least some of the ions released by the aluminosilicate into new Al-bearing phases. Similar features were also observed in the ^{27}Al spectra of MF sample. The range in chemical shift is the same reported for some aluminophosphate glasses [41] and phosphate geopolymer [17] where the resonances have been assigned to aluminium sited in an octahedron sharing corners with P-coordinated polyhedrons, so as to build up the aluminophosphate networks. Although the broad linewidth of the ^{31}P MAS spectrum impaired the unambiguous identification of a new signal between −5 to −30 ppm, as it should be expected, according to this interpretation [17], the SEM results (Fig. 8) are compatible with this model. Moreover, the deconvolution in Fig. S4, coupled with the spectrum in Fig. S3, seem to further corroborate this assignment, since the relative contribution of the new resonance increases decreasing the MgO content (i.e., less competition for phosphate). The other alternative possible scenarios offered by the literature, seem less probable. That is: the tiny ^{31}P resonance at 3 ppm reported in glasses and exhibiting proximity with a similar Al^{VI} environment [40]; the ^{31}P resonance at 5 ppm assigned to Q^0(1Al) units in a geopolymer added with P [41]; the precipitation, upon addition of ground granulated blast furnace slag to MKPC, of a new potassium aluminosilicate phase producing an analogous ^{27}Al MAS signal [11].

The small differences in the ^{29}Si MAS spectra of cement samples compared to MSWI-FA (Fig. 5) are also compatible with the partial dissolution of gehlenite (a sorosilicate displaying mainly Q^1 units at −71 ppm) and the mobilization of Si. Likewise, Si was mobilized from willemite (a nesosilicate displaying Q^0 at −66 ppm) as indicated by the XANES results (Fig. 6). By considering the deconvolution results in Fig. S5, it is possible to suggest that the Si forms preferentially amorphous silica phases, either by reprecipitation or incongruent dissolution, as proposed for phosphate-based geopolymer [11,19].

Even though the SEM-EDS measurements were not conclusive on this hypothesis, altogether, the experimental evidences from spectroscopies point to the involvement of MSWI-FA in the cement reaction, given the intrinsic local nature of the techniques employed. In Table 5, a summary of the observed and proposed reactions and the secondary products involving MSWI-FA components is provided.

4.2. Impact on the material performance and main reaction pathway

The significant reduction of heavy metals leaching observed in the cement samples (Fig. 10) agrees with a MSWI-FA participation to the binder reaction. Indeed, in addition to the expected physical encapsulation effect of the cement matrix, XANES spectra clearly indicated a chemical stabilization due to the direct reaction of MSWI-FA components (Zn-bearing phases) with phosphate. In fact, in analogy with the Ca carbonates mentioned above, hydrozincite ($Zn_5OH_6(CO_3)_2$) is likely dissolved in the initial acidic conditions and Zn can reach the supersaturation conditions needed to precipitate hydrated Zn-phosphate phases, as they exhibit very low K_{sp} (for example, $Zn_3(PO_4)_2{\cdot}4(H_2O)$, hopeite, has $K_{sp} \sim 10^{-35}$ at 25 °C) [38]. At the same time, ZnO in MSWI-FA may directly react with phosphate, as observed in Zn-phosphate dental cement [42]. Eventually, these processes are kinetically competing with the main reaction involving MgO (for K-struvite, K_{sp} is $\sim 10^{-11}$ at 25 °C), thus allowing an effective chemical immobilization [1,38].

When considering the main reaction pathway, the ICC curves indicated a marked effect on the kinetics rather than on the normalized heat released (MF0, Fig. 1). The acceleration of the second exothermic peak may be considered the effect of enhanced nucleation of the reaction products. Heterogeneous nucleation is known to be thermodynamically favoured [1]. In MKPC, this role is commonly played by MgO, as confirmed by the positive correlation between its specific surface area and the K-struvite crystallization rates [3,4]. Therefore, the high specific surface area of the ash provides additional room for nucleation of the reaction products (Fig. S7). Although less evident, a similar effect is present in MF100, since the delay of the MgO dissolution with respect to REF is not followed by a delay of the K-struvite crystallization. This behaviour can also explain the increase of the amorphous-phase/crystal-phase ratio passing from REF to MF0/100. Owing to the adoption of slower heat-exchange rate (i.e., at T of 5–15 °C), previous calorimetric studies have shown that the MKP crystallization is preceded by an exothermic event, attributed to the formation of an amorphous precursor that later converts to K-struvite, and demonstrated that their interconversion is hindered in a more kinetically driven reaction pathway, i.e., at higher reaction rate [1,2]. On the other hand, the mobilization of Al and Si by the addition of metakaolin in MKPC has been linked to an increase in the amount of amorphous fraction [14]. Although the mechanisms were not yet clarified, an analogous effect can occur here, too, since a similar release of Al and Si is observed.

In terms of compressive strength performance, the introduction of a waste in a binder may cause a decrease of the properties, due to a detrimental dilution effect [8,38]. In the case of the "inert" formulation, the comparable results (Fig. 10) suggest that the cement dilution is compensated by the precipitation of MSWI-FA secondary products and the ash good interaction with the matrix, as observed in Fig. 9. The 60 % compressive strength increase measured for MF100 (9.2 versus 15.5) is less straightforward to interpret. On one hand, an increase of MSWI-FA secondary products has been determined passing from MF0 to MF100, in terms of Al, Si and Zn SSNMR and XANES, respectively, in agreement with the results of the isocalorimetric tests conducted on the MSWI-FA in contact with the KDP solution. It is plausible that this may have contributed to strengthen the microstructure. On the other hand, significant differences in the formulation parameters are present between REF and MF100 (i.e., an *effective* M/P ratio of 1.75 and 1.23, respectively). This lower M/P ratio is thought to promote a more effective MgO dissolution, as indicated, in the isocalorimetry curves, by the higher amount of heat released in the corresponding transient time (first 10–15 min) and the higher and larger normalized heat flow peak of MF100. Indeed, the mechanical properties of the MKPC are highly dependent on the amount of water, retardant, M/P ratio, purity of MgO (i.e., industrial grade periclase that has more impurities that could improve the strength), which affect the K-struvite crystallization pathway [1,5,6]. Additional work should be done to further isolate the contribution of the MSWI-FA chemical effect on this complex reaction mechanism from other parameters, for example by coupling the investigating of pore solution composition as a function of aging time with phases equilibrium thermodynamic modelling [43,44]. Nonetheless, it is possible to propose that MSWI-FA participates through i) fast dissolution and precipitation of very low solubility products that may compete with MKP; ii) late precipitation due to pH changes and water subtraction during MKP gelification.

Overall, the results provided here suggest that the optimization of a MKPC/MSWI-FA solidification/stabilization formulation should take into account the reactivity of the ash [10].

5. Conclusions

This work reports about the investigation of the reactivity of washed MSWI-FA, introduced in magnesium potassium phosphate cement, adopting an "inert" formulation, where MWSI-FA replaces both magnesia and KDP, and a "reactive" formulation, where the waste replaces magnesia. The following conclusions can be drawn:

- SSNMR and XAS agree to indicate that, in both inert and reactive conditions, dissolution/precipitation reactions involving MSWI-FA occur. Around 30 % of Zn, the most abundant heavy metal in the waste, becomes bound to phosphate, together with Al. The dissolution of the abundant sulfate leads to the precipitation of K_2SO_4;
- The proposed mechanisms involved the fast MSWI-FA dissolution with precipitation of very low solubility phases, and the late precipitation due to pH changes and water subtraction during MKPC gelification.
- The investigation of the suspension of MSWI-FA in a KH_2PO_4 saturated solution confirmed these results and pointed to a mainly amorphous character of the reaction products;
- The introduction of MSWI-FA increases the amorphous content of MKPC, of the order of 35–50 %, as shown by ICC, XRPD and SEM observations, although the mechanism has not been delucidated.
- In both formulations, the leaching of all the investigated heavy metals has been reduced down to 70–99 %, below the Italian legal limit for inert waste, thus proving that MKPC can be a promising matrix for the encapsulation of MSWI-FA.
- The compressive strength of the inert formulation is comparable with respect to the reference, while a 60 % increase is observed for the reactive formulation. Overall, the results suggest that for an effective cement formulation, aimed at recycling MSWI-FA in MKPC, the reactivity of the fly ash must be taken into account.

Funding

The present study (AP) has been partly funded by Ministero della Transizione Ecologica through the call: "CLEAN – Ceneri Leggere Ecosostenibili per un Ambiente No-rifiuti" (m_amte.MiTE.REGISTRO UFFICIALE.USCITA.0049573.22-04-2022).

CRediT authorship contribution statement

Davide Bernasconi: Writing – review & editing, Writing – original draft, Visualization, Validation, Methodology, Investigation, Formal analysis, Data curation, Conceptualization. **Alberto Viani:** Conceptualization, Methodology, Formal Analysis, Resources, Supervision, Writing – original draft, Writing – review & editing. **Lucie Zárybnická:** Investigation, Formal Analysis, Writing – review & editing. **Petra Mácová:** Investigation, Writing – review & editing. **Simone Bordignon:** Writing – review & editing, Investigation, Formal analysis. **Gangadhar Das:** Writing – review & editing, Investigation. **Elisa Borfecchia:** Investigation, Formal analysis, Writing – review & editing. **Mateja Štefančič:** Writing – review & editing, Investigation. **Caterina Caviglia:** Investigation, Writing – review & editing. **Enrico Destefanis:** Investigation, Writing – review & editing. **Andrea Bernasconi:** Writing – review & editing, Formal analysis. **Roberto Gobetto:** Formal Analysis, Resources, Writing – review & editing. **Alessandro Pavese:** Writing – review & editing, Supervision, Resources, Project administration, Funding acquisition.

Declaration of Competing Interest

The authors declare that they have no known competing financial interests or personal relationships that could have appeared to influence the work reported in this paper.

Data availability

Data will be made available on request.

Acknowledgments

A.V., L.Z., P.M. acknowledge support from the Czech Academy of Sciences, Institute of Theoretical and Applied Mechanics (RVO 68378297) D.B. thanks Mr. Andrea Cotellucci and Mr. Quentin Wehrung for useful help and discussion during XAS experiments. E.B. acknowledges support from project n. 2017KKP5Z PRIN-2017 MOSCATo and from the Project CH4.0 under the MUR program "Dipartimenti di Eccellenza 2023-2027" (CUP: D13C22003520001). We acknowledge Elettra Sincrotrone Trieste for providing access to its synchrotron radiation facilities (proposal nr. 20215071) and for financial support under the SUI (P2022002) internal project.

Appendix A. Supplementary data

Supplementary data to this article can be found online at https://doi.org/10.1016/j.conbuildmat.2023.134082.

References

[1] A. Viani, P. Macova, Polyamorphism and frustrated crystallization in the acid-base reaction of magnesium potassium phosphate cements, CrystEngComm 20 (2018) 4600–4613.
[2] A. Viani, G. Mali, P. Macova, Investigation of amorphous and crystalline phosphates in magnesium phosphate ceramics with solid-state ^{1}H and ^{31}P NMR spectroscopy, Ceram. Int. 6571–6579 (2017).

[3] A. Viani, A. Radulescu, M. Perez-Estebanez, Characterisation and development of fine porosity in magnesium potassium phosphate ceramics, Mater. Lett. 161 (2015) 628–630.
[4] A. Viani, K. Sotiriadis, P. Sasek, M.S. Appavou, Evolution of microstructure and performance in magnesium potassium phosphate ceramics: role of sintering temperature of MgO powder, Ceram. Int. 42 (2016).
[5] H. Lahalle, C. Coumes, C. Mercier, D. Lambertin, C. Cannes, S. Delpech, S. Gauffinet, Influence of the w/c ratio on the hydration process of a magnesium phosphate cement and on its retardation by boric acid, Cem. Concr. Res. 106 (2018) 159–174.
[6] B. Xu, F. Winnefeld, J. Kaufmann, B. Lothenbach, Influence of magnesium-to-phosphate ratio and water-to-cement ratio on hydration and properties of magnesium potassium phosphate cements, Cem. Concr. Res. 106 (2019), 105781.
[7] Q. Zhang, X. Cao, R. Ma, S. Sun, L. Fang, J. Lin, J. Luo, Solid waste-based magnesium phosphate cements: Preparation, performance and solidification/stabilization mechanism, Const. Build. Mat. (2021), 123761.
[8] X. Zhou, Z.F. Zhang, C.J. Bao, Y.C. Yue, J.S. Wang, H. Yang, M.J. Chen, Y. Liu, The stabilization mechanism of high-efficiency magnesium phosphate cement for arsenic remediation in lollingite polluted environments, J. Clean. Prod. 378 (2022), 134580.
[9] C. Gong, F. Shuo, K. Xia, J. Chen, L. Guo, W. Guo, Enhancing the mechanical properties and cytocompatibility of magnesium potassium phosphate cement by incorporating oxygen-carboxymethyl chitosan, Regen. Biomat. 8 (2021) rbaa048.
[10] B.W. Xu, H.Y. Ma, H. Shao, B. Lothenbach, Influence of fly ash on compressive strength and micro-characteristics of magnesium potassium phosphate cement mortars, Cem. Concr. Res. 99 (2017) 86–94.
[11] L.J. Gardner, S.A. Bernal, S.A. Walling, C.K. Corkhill, J.L. Provis, N.C. Hyatt, Characterisation of magnesium potassium phosphate cements blended with fly ash and ground granulated blast furnace slag, Cem. Concr. Res. 74 (2015) 78–87.
[12] S. Ruan, C. Unluer, Influence of supplementary cementitious materials on the performance and environmental impacts of reactive magnesia cement concrete, J. Clean. Prod. 159 (2017) 62–73.
[13] B. Xu, B. Lothenbach, H. Ma, Properties of fly ash blended magnesium potassium phosphate mortars: effect of the ratio between fly ash and magnesia, Cem. Concr. Compos. 90 (2018) 169–177.
[14] Z. Qin, C. Ma, Z. Zheng, G. Long, B. Chen, Effects of metakaolin on properties and microstructure of magnesium phosphate cement, Const. Build. Mat. 234 (2020), 117353.
[15] H. Zhang, P. He, L.M. Shao, Fate of heavy metals during municipal solid waste incineration in Shanghai, J. Hazard. Mat. 156 (2008) 365–373.
[16] B.A.R. Ebert, B.M. Steenari, M.R. Geiker, G.M. Kirkelund, Screening of untreated municipal solid waste incineration fly ash for use in cement-based materials: chemical and physical properties, SN Appl. Sci. 2 (2020) 802.
[17] D. Bernasconi, C. Caviglia, E. Destefanis, A. Agostino, R. Boero, N. Marinoni, C. Bonadiman, A. Pavese, Influence of speciation distribution and particle size on heavy metal leaching from MSWI fly ash, Waste Manag. 138 (2022) 318–327.
[18] J. Liu, Z. Wang, G. Xie, Z. Li, X. Fan, W. Zhang, F. Xing, L. Tang, J. Ren, Resource utilization of municipal solid waste incineration fly ash - cement and alkali-activated cementitious materials: A review, Sci. Total Environ. 852 (2022), 158254.
[19] D. Bernasconi, A. Viani, L. Zarybnicka, P. Macova, S. Bordignon, C. Caviglia, E. Destefanis, R. Gobetto, A. Pavese, Phosphate-based geopolymer: Influence of municipal solid waste fly ash introduction on structure and compressive strength, Ceram. Int. 138 (2023) 318–327.
[20] X. Zhan, L. Wang, L. Wang, X. Wang, J. Gong, L. Yang, J. Bai, Enhanced geopolymeric co-disposal efficiency of heavy metals from MSWI fly ash and electrolytic manganese residue using complex alkaline and calcining pre-treatment, Waste Manag. 98 (2019) 135–143.
[21] Y. Su, J. Yang, D. Liu, S. Zhen, N. Lin, Y. Zhou, Effects of municipal solid waste incineration fly ash on solidification/stabilization of Cd and Pb by magnesium potassium phosphate cement, J. Environ. Chem. Eng. 4 (2016) 259–265.
[22] J. Yang, S. Zhen, Q. Wu, Effect of Municipal Solid Waste Incineration Fly Ash on Properties of Magnesium Potassium Phosphate Paste, J. Mat. Civil Eng. 31 (2019) 06019013.
[23] E. Destefanis, C. Caviglia, D. Bernasconi, E. Bicchi, R. Boero, C. Bonadiman, G. Confalonieri, I. Corazzari, G. Mandrone, L. Pastero, A. Pavese, F. Turci, Q. Wehrung, Valorization of mswi bottom ash as a function of particle size distribution, using steam washing, Sustainability (Switzerland) 12 (2021) 11–17.
[24] C. Caviglia, E. Destefanis, L. Pastero, D. Bernasconi, C. Bonadiman, A. Pavese, MSWI Fly Ash Multiple Washing: Kinetics of Dissolution in Water, as Function of Time, Temperature and Dilution, Minerals 12 (2022) 742.
[25] B.H. Toby, R.B. Von Dreele, GSAS-II: the genesis of a modern open-source all-purpose crystallography software package, J. Appl. Cryst. 46 (2013) 544–549.
[26] W.Y. Lin, K.S. Heng, M.Q. Nguyen, J.R.I. Ho, Evaluation of the leaching behavior of incineration bottom ash using seawater: a comparison with standard leaching tests, Waste Manag. 62 (2017) 139–146.
[27] D. Salusso, E. Borfecchia, S. Bordiga, Combining X-ray Diffraction and X-ray Absorption Spectroscopy to Unveil Zn Local Environment in Zn-Doped ZrO_2 Catalysts, J. Phys. Chem. C 125 (2021) 22249–22261.
[28] A. Wagh, S.Y. Jeong, Chemically bonded phosphate ceramics: I, a dissolution model of formation, J. Am. Ceram. Soc. 86 (2003) 1838–1844.
[29] M. Mbogoro, E. Snowden, M. Edwards, M. Peruffo, P. Unwin, Intrinsic Kinetics of Gypsum and Calcium Sulfate Anhydrite Dissolution: Surface Selective Studies under Hydrodynamic Control and the Effect of Additives, J. Phys. Chem. C 115 (2011) 10147–10154.
[30] A.P. Legrand, H. Sfihi, N. Lequeux, J. Lemaître, ^{31}P Solid-State NMR study of the chemical setting process of a dual-paste injectable brushite cements, J. Biomed. Mater. Res. 91B (2009) 46–54.
[31] J. Skibsted, M.T. Pedersen, J., Holzinger Resolution of the Two Aluminum Sites in Ettringite by 27Al MAS and MQMAS NMR at Very High Magnetic Field (22.3 T), J. Phys. Chem. C 21 (2017) 4011–4017.
[32] M. Edén, NMR studies of oxide-based glasses, Annu. Rep. Prog. Chem., Sect. C: Phys. Chem. 108 (2012) 177–221.
[33] A. Martini, E. Borfecchia, Spectral Decomposition of X-ray Absorption Spectroscopy Datasets: Methods and Applications, Crystals 10 (2020) 664.
[34] I.J. Godfrey, A.J. Dent, I.P. Parkin, S. Maenosono, G. Sankar, Following the Formation of Silver Nanoparticles Using In Situ X-ray Absorption Spectroscopy, ACS Omega 5 (2020) 13664–13671.
[35] I. Pinilla-Herrero, E. Borfecchia, T. Cordero-Lanzac, U.V. Mentzel, F. Joensen, K. A. Lomachenko, S. Bordiga, U. Olsbye, P. Beato, S. Svelle, Finding the active species: The conversion of methanol to aromatics over Zn-ZSM-5/alumina shaped catalysts, J. Catal. 394 (394) (2021) 416–428.
[36] A. Viani, P. Macova, K. Sotiriadis, Amorphous-crystalline transformation control on the microstructural evolution of magnesium phosphate cements, Mater. Lett. 129630 (2021).
[37] H. Ma, Y. Li, Discussion of the paper “Characterisation of magnesium potassium phosphate cement blended with fly ash and ground granulated blast furnace slag” by L.J. Gardner et al, Cem. Concr. Res. (2018) 245–248.
[38] Y. Zhang, Z. Wan, L. Wang, B. Guo, B. Ma, L. Chen, D.C.W. Tsang, Designing Magnesium Phosphate Cement for Stabilization/Solidification of Zn-Rich Electroplating Sludge, Environ. Sci. Tech. 56 (2022) 9398–9407.
[39] G.U. Ministerial Decree 27/09/2010-Definition of the Criteria of Admissibility of Landfill Waste. Serie Generale n-281. 1 December 2010. Available online: https://www.gazzettaufficiale.it/eli/id/2010/12/01/10A14538/sg.
[40] S. Wegner, L. van Wullen, G. Tricot, The structure of aluminophosphate glasses revisited: Application of modern solid state NMR strategies to determine structural motifs on intermediate length scales, J. Non-Cryst. Sol. 356 (2008) 1703–1715.
[41] A. Gharzouni, I. Sobrados, N. Texier-Mandoki, X. Bourbon, S. Rossignol, ^{29}Si, ^{27}Al, ^{31}P and ^{11}B magic angle spinning nuclear magnetic resonance study of the structural evolutions induced by the use of phosphor- and boron–based additives in geopolymer mixtures J. Non-Cryst. Sol. (2019) 119541.
[42] A. Viani, K. Sotiriadis, I. Kumpová, L. Mancini, M.S. Appavou, Microstructural characterization of dental zinc phosphate cements using combined small angle neutron scattering and microfocus X-ray computed tomography, Dent Mater. 33 (2017) 402–417.
[43] T. Honorio, F. Benboudjema, T. Bore, M. Ferhat, E. Vourc’h, The pore solution of cement-based materials: structure and dynamics of water and ions from molecular simulations, Phys. Chem. Chem. Phys. 21 (2019) 11111–11121.
[44] H. Lahalle, C. Patapy, M. Glid, G. Renaudin, M. Cyr, Microstructural evolution/durability of magnesium phosphate cement paste over time in neutral and basic environments, Cem. Concr. Res. 122 (2019) 42–58.